ACS NANO

www.acsnano.org

ARTICLE

Strain-Induced Reversible Motion of Skyrmions at Room Temperature

Chen Liu, Junlin Wang, Wa He, Chenhui Zhang, Senfu Zhang, Shuai Yuan, Zhipeng Hou,* Minghui Qin, Yongbing Xu, Xingsen Gao, Yong Peng,* Kai Liu, Zi Qiang Qiu, Jun-Ming Liu, and Xixiang Zhang*

Cite This: *ACS Nano* 2024, 18, 761−769

Read Online

ACCESS | Metrics & More | Article Recommendations | Supporting Information

ABSTRACT: **Magnetic skyrmions are topologically protected swirling spin textures with great potential for future spintronic applications. The ability to induce skyrmion motion using mechanical strain not only stimulates the exploration of exotic physics but also affords the opportunity to develop energy-efficient spintronic devices. However, the experimental realization of strain-driven skyrmion motion remains a formidable challenge. Herein, we demonstrate that the inhomogeneous uniaxial compressive strain can induce the movement of isolated skyrmions from regions of high strain to regions of low strain at room temperature, which was directly observed using an *in situ* Lorentz transmission electron microscope with a specially designed nanoindentation holder. We discover that the uniaxial compressive strain can transform skyrmions into a single domain with in-plane magnetization, resulting in the coexistence of skyrmions with a single domain along the direction of the strain gradient. Through comprehensive micromagnetic simulations, we reveal that the repulsive interactions between skyrmions and the single domain serve as the driving force behind the skyrmion motion. The precise control of skyrmion motion through strain provides exciting opportunities for designing advanced spintronic devices that leverage the intricate interplay between strain and magnetism.**

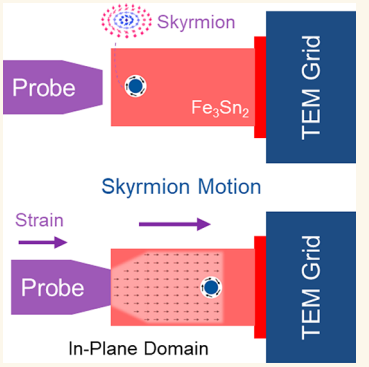

KEYWORDS: *magnetic skyrmions, room temperature, strain, magnetic anisotropy, Fe_3Sn_2*

1. INTRODUCTION

Over the past decade, magnetic skyrmions, which are vortex-like swirling spin configurations, have undergone significant advancements due to their intriguing physics and potential applications as information carriers for future spintronic devices, such as racetrack memories.[1,2] Skyrmions are typically observed in noncentrosymmetric chiral crystals[3−5] and asymmetric magnetic films.[6,7] In these magnetic systems, the breaking of the crystal symmetry causes the emergence of a Dzyaloshinskii−Moriya interaction (DMI) that not only stabilizes the skyrmions but also locks their helicity. In addition to the DMI-hosting magnetic systems, centrosymmetric ferromagnets can stabilize skyrmions through the interplay of magnetic anisotropy and dipole−dipole interaction.[8−11] Due to the absence of a DMI, these topological spin configurations exhibit random helicity and multiple spin textures. However, from a topological perspective, skyrmions in both the noncentrosymmetric and centrosymmetric material systems are topologically equivalent and share similar topological magnetoelectrical properties, such as the skyrmion Hall effect,[12,13] topological Hall effect,[14−16] and ultralow driving current density for motion.[17−19]

For practical applications of skyrmionic devices, the controllable manipulation and directional movement of skyrmions under external stimuli are crucial. Currently, these operations primarily rely on spin-polarized current.[19−25] However, the current density required for these operations is extraordinarily high, leading to substantial energy consumption.[25] Moreover, Joule heating generated by the current poses a considerable challenge to the structural stability of skyrmions. To reduce the energy consumption and Joule heating of skyrmionic devices, various operating schemes, such as gate voltage,[26−29] ultrafast laser pulse,[30] magnons,[31] thermal excitations,[32] and adsorption/desorption,[33,34] have been theoretically proposed or experimentally realized. In addition to these approaches, increasing attention has been focused on the strain-based strategy, driven not only by its low energy consumption but also by the intriguing magnetoelastic responses.[35−48] One of the notable examples is that Shibata et al. found a low anisotropic uniaxial strain of 0.3% could induce a 20% distortion in its skyrmion

Received: September 20, 2023
Revised: December 8, 2023
Accepted: December 19, 2023
Published: December 21, 2023

https://doi.org/10.1021/acsnano.3c09090
ACS Nano 2024, 18, 761−769

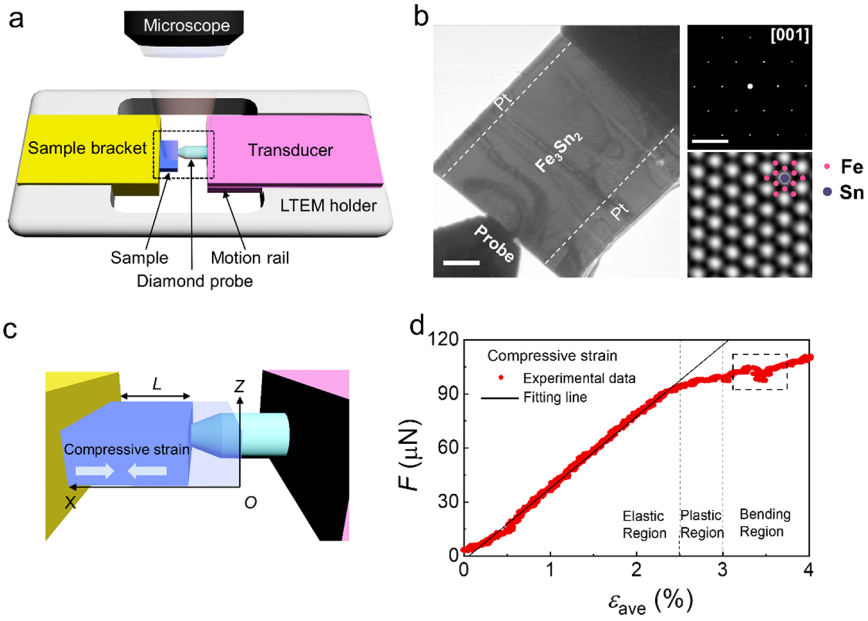

Figure 1. Structure of the working region of the strain-holder and stress dependence on the average strain. (a) Schematic of the working region of the holder. (b) LTEM image of the working region (left panel). The scale bar is 500 nm. The upper right panel represents the SAED pattern along the normal direction of the Fe_3Sn_2 thin plate. The scale bar is 5 1/nm. The lower right panel represents the HR-STEM image of the Fe_3Sn_2 thin plate. The inset in the right bottom panel shows the alternating arrangement of Fe (red particle) and Sn atoms (blue particles). (c) Schematic for applying compressive strain on a sample. The length (L) of the sample is along the x-axis, and the thickness (t) is along the z-axis. The sample is compressed along the x-axis by moving the probe. The original point (o) represents the location of the sample when it is not compressed. Δx represents the moving distance of the probe and the compressive distance of the sample. (d) The stress (F) dependence on the average compressive strain (ε_{ave}). The curve is fitted using a linear equation (black line). The dashed box shows a kink in the F–ε_{ave} curve. The dashed line represents the boundary of the deformation in the Fe_3Sn_2 thin plate. The boundaries from the left to the right represent the stress results for elastic deformation, plastic deformation, and bending of the sample.

lattice along the strain axis in the chiral crystal FeGe.[35] More recently, Hou et al. demonstrated that strain could trigger controllable four-state switching of the number of skyrmions in geometrically confined nanodots.[36] These reactions of skyrmions to the uniaxial strain demonstrate promising potential for constructing strain-mediated spintronic devices, including flexible and microwave devices.[49] Nevertheless, despite these advances, the strain-induced directional motion of skyrmions, which is crucial for constructing racetrack memory devices, remains elusive in experiments. The main challenge lies in generating the driving force necessary for inducing skyrmion motion. This is because strain lacks the inherent capability to transport the polarized spins that typically drive skyrmion motion through spin-transfer torque (STT) or spin-orbit torque (SOT) effects. On the other hand, this study necessitates the precise measurement of nanometric magnetic domain structures within nanomaterials while simultaneously enabling localized control over strain,[50] which poses a technical obstacle in observing the strain-induced motion of skyrmions.

In this study, we target room-temperature skyrmion-hosting ferromagnet Fe_3Sn_2 and demonstrate that the inhomogeneous uniaxial compressive strain can induce the movement of isolated skyrmions from regions of high strain to regions of low strain at room temperature, which was directly observed using *in situ* Lorentz transmission electron microscopy (LTEM). We discover that the uniaxial compressive strain can induce the transformation of skyrmions into a single domain with in-plane magnetization, resulting in the coexistence of skyrmions with a single domain along the direction of the strain gradient. Combining with micromagnetic simulations, we further reveal that the repulsive interactions between skyrmions and the single domain serve as the driving force behind the skyrmion motion. Our results provide valuable insights into the underlying physical mechanism of the strain-induced dynamics of skyrmions and highlight their promising potential in the development of low-power, strain-sensitive spintronic devices.

2. RESULTS

2.1. Fabrication of a Strain-Mediated Device for *In Situ* LTEM Observations. The target ferromagnet Fe_3Sn_2 has a centrosymmetric rhombohedral structure with alternate stacking of Fe–Sn kagome layers along the z-axis. Our previous investigations have demonstrated that this compound could host skyrmions over an extremely wide range of temperatures from 100 to 630 K.[8] The high thermal stability makes Fe_3Sn_2 an attractive platform for studying the fundamental physics and practical applications of skyrmions. To investigate the strain-induced dynamic behaviors of skyrmions, we conducted *in situ* LTEM experiments using a specially designed nanoindentation holder. Figure 1a schematically illustrates the working region of the holder, consisting of a sample bracket and a diamond probe (circular shape with a diameter of ~700 nm) with a strain transducer. Using focused ion beam (FIB) techniques, a [001]-oriented Fe_3Sn_2 lamella (length $l \approx 2.4$ μm, width $w \approx 1.5$ μm, thickness $t \approx 150$ nm) was prepared and securely mounted on the sample bracket for LTEM observations (Figure 1b). Notably, the outer region of the lamella was coated with a Pt protection layer against ion beam damage during the fabrication process. Further details regarding the fabrication process can be found in the Methods. Selected-area electron diffraction (SAED) was performed along the normal direction of the lamella. The resulting diffraction spots (upper right panel of

https://doi.org/10.1021/acsnano.3c09090
ACS Nano 2024, 18, 761–769

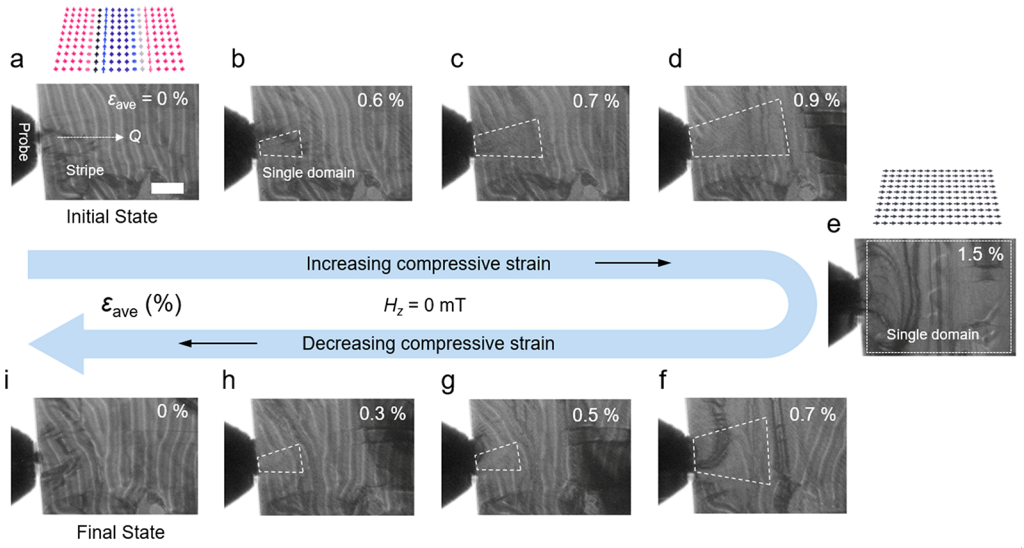

Figure 2. Strain-induced domain evolution process at H_z = 0 mT. The upper panel of (a) is the schematic for the spin texture of the stripe domain. The lower panel of (a) is an LTEM image of the thin plate in the initial state, i.e., H_z = 0 mT and ε_{ave} = 0%. The white dashed arrow represents the orientation of the wave vector (Q) of the stripe domain. The upper panel shows the schematic of the Bloch stripe domain wall. (b−e) LTEM images of the thin plate at ε_{ave} = 0.6, 0.7, 0.9, and 1.5%, respectively. The region enclosed by the white dashed boxes hosts a single domain with in-plane magnetization. The upper panel of (e) represents the spin arrangements of a single domain. (f−i) LTEM images of the thin plate at ε_{ave} = 0.7, 0.5, 0.3, and 0% (final state), respectively. All the images are taken at H_z = 0 mT. The scale bar for all of the images is presented in (a), and it represents 500 nm.

Figure 1b) exhibited a sixfold symmetric characteristic, confirming that the normal direction of the lamella aligns with the [001] orientation. Additionally, a high-angle annular dark-field scanning transmission electron microscopy (HAADF-STEM) image obtained at the (001) crystal plane (lower right panel of Figure 1b) demonstrated the Fe (red particles) and Sn atoms (blue particles) orderly arranged into the kagome lattice. This observation agrees well with the (001) crystal plane of Fe_3Sn_2, indicating good quality of the lamella.

Compressive stress can be applied to the Fe_3Sn_2 lamella by moving the diamond probe along the rail (Figure 1c). Given the probe's extensive range of movement in the *xyz* directions and its tip thickness of approximately 700 nm, significantly thicker than the lamella, aligning the lamella and the probe to the same height becomes easily achievable. This alignment effectively mitigates the risk of bending when a stress is applied. The stress compresses the crystal lattice, thereby inducing a uniaxial compressive strain (ε) along the indentation direction. The stress strength (F) and the moving distance (Δx) of the probe are accurately and promptly recorded by the transducer. Taking the position of the probe just starting to get in touch with the lamella as its initial position, Δx can be approximately assumed as the compressive distance of the lamella. Some factors that may influence this assumption, such as the contact area between the probe and lamella, welding materials deposited to mount the lamella, and whether the lamella is bending, were discussed in Supplementary Notes. The average strength of the compressive strain (ε_{ave}) can be calculated using the following equation:

$$\varepsilon_{ave} = \frac{\Delta x}{L_0} \quad (1)$$

where L_0 represents the length of the lamella (Figure 1c). In Figure 1d, the variation in F is plotted as a function of ε_{ave}. It is demonstrated that F linearly increased as ε_{ave} increased from the initial state (ε_{ave} = 0%) to 2.4%. The linear relation between ε_{ave} and F obeyed Hooke's law, indicating that the stress generated an elastic deformation in the lamella. As ε_{ave} increased beyond 2.4% and up to 3%, the ε_{ave}−F curve gradually deviated from the linear dependence of Hooke's law, suggesting that the deformation gradually transformed from elastic into plastic behavior under large strains. With a further increase in ε_{ave}, a kink appeared in the ε_{ave}−F curve (enclosed by a dashed box in Figure 1d). This abnormal transition is generally regarded as the bending signature of a thin plate. To prevent the plastic deformation and bending of the sample from affecting the experimental results, we thus limited the maximum ε_{ave} to less than 2.4% in subsequent measurements.

2.2. Strain-Induced Dynamics of the Magnetic Domains. First, we studied the strain-induced domain evolution without applying any magnetic field (based on a fresh sample with a similar dimension to that displayed in Figure 1b). The strain was gradually and linearly increased from zero to the maximum value (ε_{ave} = 1.5%) at a specific velocity of 0.15% per second. Simultaneously, the dynamic behaviors of the domain structures were recorded as movies at 25 frames per second. Figure 2a−i presents a series of snapshots extracted from Movie S1 to illustrate the detailed domain evolution processes. In the initial state (ε_{ave} = 0%), the lamella exhibited nanosized stripe domains (as schematically illustrated in the left panel of Figure 2a) with their wave vector (Q) along the length direction (lower panel of Figure 2a). Although no considerable motion of the stripes was observed as the average strain (ε_{ave}) gradually increased to 0.6%, the stripe domains near the probe (enclosed by the white dashed box) disappeared (Figure 2b). This observation suggests that under strain, the stripe domains transformed into a single domain that does not exhibit a distinct contrast in the LTEM image (Figure S1). However, apart from the region near the probe, the stripe domains in the remaining portion of the lamella hardly changed, indicating that the strain was distributed with a gradient. With a further increase in ε_{ave}, the single domain expanded gradually along the length direction of the lamella (Figure 2c,d). When ε_{ave} increased up to 1.5%, the

https://doi.org/10.1021/acsnano.3c09090
ACS Nano 2024, 18, 761−769

stripe domains completely disappeared (lower panel of Figure 2e). Conversely, as ε_{ave} decreased, the size of the single domain decreased, which was accompanied by the recovery of the stripe domains (Figure 2e–i). Because the formation of the single domain was induced by the applied strain, the extension direction of the single domain reflected the strain distribution induced by the applied strain. Specifically, the strain near the probe was the largest and gradually decreased from the region near the probe toward the right edge (along the $+x$ direction). It should be noted that the direct quantitative measurement of the nonuniform strain distribution on the microsized lamella was challenging by analyzing SAED patterns under each strain value (see Supplementary Notes and Figure S2 for details). Phase-field simulations were thus performed to estimate the strain distribution. Details about the simulations can be found in Figure S3. The simulated strain distribution exhibited a gradient distribution on the lamella and decreased gradually along the length direction. This was consistent with the experimental observations, thereby confirming the reliability of our simulations.

We further revealed that the magnetization of the single domain aligned in the xy-plane based on theoretical analysis. From an energy perspective, the equilibrium magnetic state of the Fe_3Sn_2 lamella subjected to a coupled magnetoelastic loading is determined by minimizing the Helmholtz free energy described by the following equation:

$$F = \int \left[A(\nabla \mathbf{M})^2 + \omega_{DDI} - K_u M_z^2 - \frac{1}{2}\mu_0 M_s \mathbf{H}\cdot\mathbf{M} + \omega_{ME} \right] dV \quad (2)$$

where the term in the integrand denotes the volumetric densities ($J\cdot m^{-3}$), A represents the exchange stiffness, ω_{DDI} represents the dipole–dipole energy density (i.e., the demagnetization energy density), K_u represents the uniaxial anisotropy constant along the z-axis (c-axis of Fe_3Sn_2), $\mathbf{M}$ represents the unit vector of magnetization, $\mathbf{H}$ represents the external magnetic field, and ω_{ME} represents the magnetoelastic free energy density when the system is subjected to a uniaxial tension–compression along the x-axis. Since Fe_3Sn_2 belongs to the point group D_{3d}, the term ω_{ME} can be expressed as follows:

$$\omega_{ME} = \varepsilon_{11}(d_{1111}M_x^2 + d_{1122}M_y^2 + d_{1133}M_z^2 + 2d_{1123}M_yM_z) \quad (3)$$

where d_{1111}, d_{1122}, d_{1133}, and d_{1123} represent the tensor forms of the magnetoelastic coefficients. For magnetoelastic coupling, we generally have $d_{1111} > d_{1122} \approx d_{1133} \gg d_{1123}$.[37,38] Thus, eq 3 can be further simplified as follows:

$$\omega_{ME} = \varepsilon_{11}(c + L_1M_x^2 + L_2M_z^2) \quad (4)$$

where $c = d_{1122}\mathbf{M}^2$ denotes a constant, and $L_1 = d_{1111} - d_{1122}$, $L_2 = d_{1133} - d_{1122}$. After eq 4 is substituted into eq 2, the free energy can be further expressed as follows:

$$F = \int \left[A(\nabla \mathbf{M})^2 + \omega_{DDI} - K_u^*(\varepsilon_{11})M_\varepsilon^2 - \frac{1}{2}\mu_0 M_s \mathbf{B}\cdot\mathbf{M} + \varepsilon_{11}c \right] dV \quad (5)$$

where M_ε represents the magnetization component in the direction of the strain-modified uniaxial anisotropy, and the absolute value of $K_u^*(\varepsilon_{xx})$ is equal to

$$|K_u^*(\varepsilon_{xx})| = \sqrt{(K_u - \varepsilon_{xx}L_2)^2 + (\varepsilon_{xx}L_1)^2} \quad (6)$$

Similar to eq 2, the term $-K_u^*(\varepsilon_{11})M_\varepsilon^2$ in eq 5 has an expression similar to that of the uniaxial anisotropy energy term. Consequently, $K_u^*(\varepsilon_{xx})$ can be considered as the effective magnetic anisotropy constant that is directly coupled with the applied strain. Furthermore, using eqs 5 and 6, we found that the uniaxial strain applied along the x-axis also modified the direction of the uniaxial anisotropy. That is, the magnetic easy-axis gradually rotated from the z-axis to the x-axis with an increasing compressive strain. Thus, we propose that the spins of the single domain displayed in Figure 2b–h were aligned along the x-axis in the xy-plane. Namely, the strain has transformed the stripe domain into the single domain with magnetization along the x-axis in the xy-plane, as schematically shown in the upper panel of Figure 2e.

2.3. Strain-Induced Dynamics of the Magnetic Skyrmions. We then explored the dynamics of skyrmions under strains. To facilitate the formation of skyrmions, an out-of-plane magnetic field (H_z) of 250 mT was applied. Figure 3a shows a representative LTEM image of the Fe_3Sn_2 lamella. It is evident that the stripe domains have completely transformed into skyrmions that are densely arranged in the xy-plane. Interestingly, some skyrmions exhibit an inverse contrast, as indicated by the dashed box in Figure 3a. A comparison of the experimental observations and simulations reveals that the inversed contrast arises from the opposite helicity, i.e., the swirling direction of the in-plane component of the spins in the skyrmions (Figure S4). Notably, random helicity is one of the characteristics of the skyrmions that were formed in centrosymmetric magnetic systems in which DMI did not exist.[8−11] The strain-induced dynamics of the densely arranged skyrmions were recorded in Movie S2. Although a strain gradient was applied to the lamella, no obvious skyrmion motion was observed over the entire strain range (the maximum ε_{ave} = 1.5%). The motionless skyrmions can be attributed to the strong

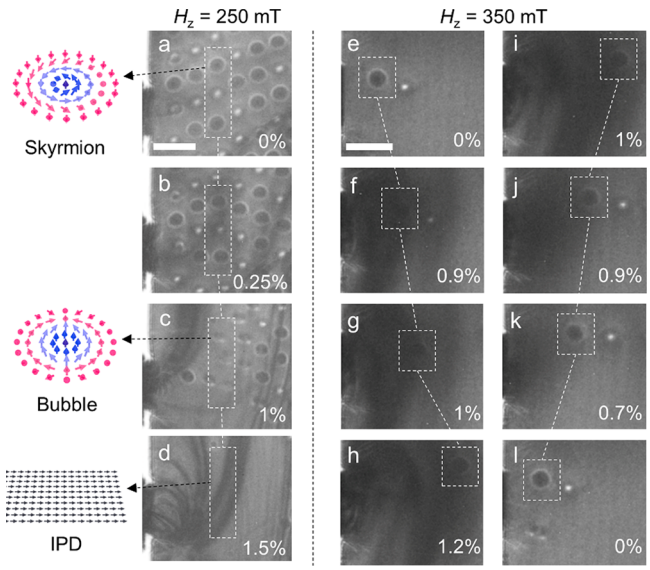

Figure 3. Strain-induced dynamic behaviors of skyrmions. The left panel of (a) is the schematic of the spin texture of the skyrmions marked by a black dashed arrow. The right panel of (a) is the LTEM image of the lamella in the initial state, i.e., H_z = 250 mT and ε_{ave} = 0%. (b–d) LTEM images of the lamella at ε_{ave} = 0.25, 1, and 1.5%, respectively. The left panels of (c) and (d) are schematics for the spin texture of the trivial bubble and the in-plane single domain, respectively. (e–l) LTEM images of the lamella at ε_{ave} = 0, 0.9, 1, 1.2, 1, 0.9, 0.7, and 0%. The magnetic domains enclosed by white boxes in (a–l) depict a one-to-one correspondence. The scale bars in (a) and (e) represent 500 nm.

https://doi.org/10.1021/acsnano.3c09090
ACS Nano 2024, 18, 761−769

pinning effect that results from the repulsive interactions among the densely arranged skyrmions. Instead of mobile skyrmions, a multistep transformation from skyrmions to in-plane single-domain structures was observed. Figure 3a−c presents a series of snapshots extracted from Movie S2 to illustrate the detailed evolution processes. As ε_{ave} increased from zero, the skyrmions first transformed into particle-like magnetic structures that exhibited distinct bright and dark contrasts at their opposite edges without tilting the sample (enclosed by a white dashed box in the right panel of Figure 3c). Combining experiments with micromagnetic simulations (see details in our previous reports[8]), we revealed that these particle-like magnetic structures are topologically trivial bubbles (the topological number is zero, as schematically shown in the left panel of Figure 3c). As ε_{ave} increased further to the maximum of 1.5%, the trivial bubbles completely transformed into an in-plane single domain (as schematically shown in the left panel of Figure 3d). The observed skyrmion → bubble → single domain transition is proposed to be closely related to the strain-induced variation in magnetic anisotropy, and a detailed explanation of the underlying mechanism is presented in the latter section.

To weaken the pinning effect caused by skyrmion−skyrmion interactions, H_z was increased from 250 to 350 mT, causing the transformation of the skyrmion lattice into isolated skyrmions. Interestingly, the compressive strain became capable of driving the motion of the individual skyrmions. With the time-resolution capability of LTEM movies, the motion of the isolated skyrmions in response to the varying applied strain was recorded (Movie S3). The LTEM images, which were extracted from Movie S3 and shown in Figure 3e−l, illustrate the trajectory of the individual skyrmions as the applied strain varied. The white boxes in Figure 3e−l indicate the corresponding positions of the same skyrmion at each strain value. It is evident that as ε_{ave} increases, the skyrmion moves from the high-strain region (left side) to the low-strain region (right side), as shown in Figure 3e−h. More interestingly, the motion of the skyrmion induced by the applied strain is discrete, implying that the skyrmion moves only when the compressive strain reaches a certain threshold value. However, if a fixed strain is applied to the sample, then the skyrmion remains stationary. This characteristic indicates that the strain-induced motion of a skyrmion occurs in a step-by-step manner, where the compressive strain must exceed a critical value at specific positions to overcome the pinning effect and subsequently initiate skyrmion motion. As the skyrmions approached the region near the right edge of the lamella, they encountered a repulsive force from the edge, causing them to halt. Notably, when ε_{ave} was decreased, the skyrmions reversed their direction of motion and moved back toward the left side (Figure 3i−l). Eventually, at ε_{ave} = 0%, the skyrmions returned to their initial positions (Figure 3l). These results reveal that the strain-induced skyrmion motion is reversible, which is highly desirable for the construction of strain-mediated racetrack memory devices.

3. DISCUSSIONS

Next, we discuss the physical mechanism that underlies the strain-induced dynamics of skyrmions. Our experimental results have demonstrated that as ε_{ave} increases, the magnetic easy-axis of Fe_3Sn_2 gradually rotates from the z-axis toward the in-plane direction, which is thought to be the main reason for the observed dynamic behaviors. To validate the proposed physical mechanism and better understand the strain-induced skyrmionic dynamics, we performed micromagnetic simulations using the physical parameters of Fe_3Sn_2 that have been established in previous experiments (see Methods for details about the simulations). First, the effect of anisotropy variation on the stabilization of a strongly pinning skyrmion was simulated (Figure S5). It was observed that as the magnetic easy-axis rotated from the z-axis toward the xy-plane, the core ($-z$) and surrounding ($+z$) magnetizations tilted toward the $+x$ direction, making the skyrmion gradually transform into a topologically trivial bubble. In this scenario, the domain walls that have in-plane magnetization along the $+x$ axis change from 180° walls to <180° walls, while the domain walls that have in-plane magnetization in the $-x$-axis change from 180° walls to >180° walls; when the latter switches their in-plane magnetization direction from $-x$ to $+x$, the whole chiral domain walls in the skyrmion (winding number = 1) change by breaking into two segments, leading to the winding number of the domain wall to be 0 and the formation of the trivial bubbles. As the magnetic easy-axis continued to rotate, the spins aligned into the xy-plane, which caused the trivial bubbles to further transform into an in-plane single domain. The simulated skyrmion → bubble → single domain transition is consistent with the experimental observations and confirms the reliability of the proposed physical model.

Hereafter, the effect of anisotropy variation on the skyrmion motion was simulated. In the simulation, a qualitative approach was used to account for the inhomogeneous strain distribution on the microsized lamella and to overcome the challenge of quantitatively measuring the strain-dependent magnetic anisotropy distribution. It was qualitatively proposed that the tilt angle (θ) between the magnetic easy-axis and the c-axis was directly proportional to the strength of ε_{ave}, while the absolute value of K_u was fixed at 1.4×10^5 J m^{-3}. Based on the simulated strain distribution, the corresponding θ distribution for different ε_{ave} values was obtained. A larger θ represents a larger strain, as schematically shown in Figure 4a. At the initial state (ε_{ave} = 0%), an isolated skyrmion was located in the middle region of the lamella (Figure 4b). With an increase in ε_{ave}, the skyrmion correspondingly moved along the $+x$ direction (Figure 4c−g). In previous theoretical studies,[51,52] the anisotropy gradient was generally suggested to act as a direct propelling force that drives skyrmions to move from regions with high anisotropy to regions with low anisotropy with a velocity proportional to the absolute value of the anisotropy gradient. According to this model, the skyrmions are expected to move along the $-x$ direction, which is opposite the motion direction observed in our experiments. This discrepancy suggests the existence of another factor influencing the skyrmion motion. As for the experiments, we found that the region hosting the in-plane single domain expanded along the $+x$ direction with the increase in ε_{ave}, as shown in Figure 4c−g. When we decreased ε_{ave}, the region hosting the in-plane domain decreased, and the skyrmion began to move along the $-x$ direction (Figure 4i−m). This observation suggests a close relationship between the motion of skyrmions and variation in the region hosting the in-plane domain. It is known that there is a repulsive potential between a skyrmion and its adjacent domain wall.[53] When the in-plane single domain expands, the repulsive potential generates a strong driving force that promotes the skyrmion motion along the $+x$ direction, corresponding to an increase in K_u. Conversely, when the region hosting the in-plane domain decreases, the repulsive force weakens, and the driving force originating from the anisotropy gradient drives the skyrmion motion along the -x direction, corresponding to a

https://doi.org/10.1021/acsnano.3c09090
ACS Nano 2024, 18, 761−769

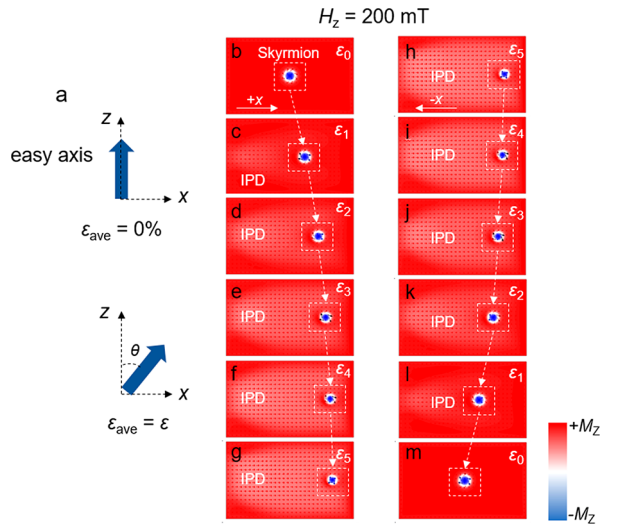

Figure 4. Simulated reversible motion of skyrmions. (a) Schematic for the angle (θ) between the z-axis (c-axis of Fe_3Sn_2) and the magnetic easy-axis (blue arrow). At the initial state (ε_{ave} = 0%), the magnetic easy-axis is parallel to the z-axis (θ = 0°), as shown in the upper panel of (a). When a compressive strain ($\varepsilon_{ave} = \varepsilon$) is applied along the x-axis, the magnetic easy-axis rotates toward the x-axis, as shown in the lower panel of (a). (b–g) Snapshots at ε_0, ε_1, ε_2, ε_3, ε_4, and ε_5. (h–m) Snapshots at ε_5, ε_4, ε_3, ε_2, ε_1, and ε_0. The external magnetic field in (b–m) is H_z = 200 mT. The magnetization along the z-axis (m_z) is represented by regions in blue ($+m_z$) and red ($-m_z$).

decrease in K_u. The simulated variation of skyrmion velocity based on this physical model is shown in Figure S6. The repulsive potential between the in-plane domains and the skyrmion drives the skyrmion to move along the $+x$ direction with an initial velocity of v_0. The strain-induced inhomogeneous anisotropic gradient causes the velocity of the skyrmion to decrease approximately in an exponential manner until it halts.

In conclusion, we have realized the controllable and reversible motion of isolated skyrmions by using both compressive strain and an out-of-plane magnetic field. The experimental results are in good agreement with the micromagnetic simulations. We revealed that the rotation of the magnetic easy-axis from the out-of-plane to the in-plane direction leads to the formation of an in-plane single domain and that the repulsive interactions between the skyrmion and the in-plane single domain provide the driving force for the skyrmion motion. Furthermore, this model was well confirmed by micromagnetic simulations. Thus, this study not only contributes to a deeper understanding of the interplay among strain, magnetic anisotropy, and domain structures but also demonstrates a promising route for developing low-power, strain-sensitive spintronic devices.

4. METHODS

4.1. Fabrication of Fe_3Sn_2 Microdevices. High-quality Fe_3Sn_2 crystals were grown using a flux method.[8] For the strain-mediated device, the lamellae with a thickness of ~150 nm were fabricated using an FIB equipped with a scanning electron microscopy dual beam system (FEI Helios G4 UX), as described in our previous work.[17] Then, the grid was fixed on the sample bracket, as shown in Figure 1a.

4.2. *In Situ* TEM Measurements. The high-resolution HAADF-STEM image and SAED pattern were obtained using TEM (FEI Titan Themis G2) with a probe corrector at an acceleration voltage of 300 kV. Skyrmions and other domain structures in the Fe_3Sn_2 lamella were observed using an FEI Tecnai F30 under Lorentz–Fresnel mode. The objective lens was switched off before the sample was loaded into the TEM. The external vertical magnetic field was applied by slowly increasing the Lorentz lens current. To achieve *in situ* strain modulation, a single-tilt *in situ* strain-holder (Hysitron PI95) was used, as shown in Figure 1a. The strain-induced dynamics was measured at room temperature.

4.3. Micromagnetic Simulations of the Domain Dynamics. Micromagnetic simulations were performed using the Mumax3 software[54] package based on the Landau–Lifshitz–Gilbert equation. For the strain-induced magnetic skyrmion dynamics in the Fe_3Sn_2 lamella, a 1250 × 500 × 150 nm^3 system was considered. The mesh size of the system was fixed at 2.5 × 2.5 × 2.5 nm^3. The strain was considered as various anisotropy direction distributions in the system. The saturation magnetization (M_s), exchange strength A, and uniaxial anisotropy K_u were selected as 5.66 × 10^5 A·m^{-1}, 1.66 × 10^{-11} J·m^{-1}, and 1.4 × 10^5 J·m^3, respectively. The external magnetic field was set at 200 mT along the perpendicular direction of the lamella. The relationship between strain ε and the tilt angle (θ) between the magnetic easy-axis is given by an assumed constant β, which is stated as $\theta = \varepsilon \times \beta$. The β is set as 20/180 in the micromagnetic simulation.

ASSOCIATED CONTENT

Supporting Information

The Supporting Information is available free of charge at https://pubs.acs.org/doi/10.1021/acsnano.3c09090.

Supplementary Notes discussing the details of the phase field, LTEM contrast simulations, possible influences on the compressive distance, SAED patterns under different strains, diffraction contrasts in Figure 3e-l, and micromagnetic simulations. Figure S1. Experimental and simulated LTEM image of domain structures in the Fe_3Sn_2 lamella. Figure S2. Variation of the SAED pattern under the strain. Figure S3. Finite element contour plots of strain distribution in the Fe_3Sn_2 lamella. Figure S4. Bloch skyrmions with opposite helicity in Fe_3Sn_2 under 250 mT fields. Figure S5. Simulated transition evolution between skyrmion and single domain with anisotropy K_u change. Figure S6. Evolution of the velocity of the skyrmion motion along the $+x$ direction with time (PDF)

Movie S1. Strain-induced stripe domain evolution process at zero external fields (MP4)

Movie S2. Strain-induced topological transformation of skyrmion lattices under 250 mT fields (MP4)

Movie S3. Strain-induced motion of a single skyrmion under 350 mT fields (MP4)

AUTHOR INFORMATION

Corresponding Authors

Zhipeng Hou − *Guangdong Provincial Key Laboratory of Optical Information Materials and Technology & Institute for Advanced Materials, South China Academy of Advanced Optoelectronics, South China Normal University, Guangzhou 510006, P. R. China;* orcid.org/0000-0003-4935-2149; Email: houzp@m.scnu.edu.cn

Yong Peng − *Key Laboratory for Magnetism and Magnetic Materials of Ministry of Education, Lanzhou University, Lanzhou 730000, P. R. China;* orcid.org/0000-0002-6980-4694; Email: pengy@lzu.edu.cn

Xixiang Zhang − *Physical Science and Engineering Division, King Abdullah University of Science and Technology, Thuwal 23955-6900, Saudi Arabia;* orcid.org/0000-0002-3478-6414; Email: xixiang.zhang@kaust.edu.sa

https://doi.org/10.1021/acsnano.3c09090
ACS Nano 2024, 18, 761–769

Authors

Chen Liu − *Physical Science and Engineering Division, King Abdullah University of Science and Technology, Thuwal 23955-6900, Saudi Arabia; Key Laboratory for Magnetism and Magnetic Materials of Ministry of Education, Lanzhou University, Lanzhou 730000, P. R. China*

Junlin Wang − *School of Integrated Circuits, Guangdong University of Technology, Guangzhou 510006, China; School of Physics, Engineering and Technology, University of York, York YO10 5DD, U.K.*

Wa He − *Key Laboratory for Magnetism and Magnetic Materials of Ministry of Education, Lanzhou University, Lanzhou 730000, P. R. China*

Chenhui Zhang − *Physical Science and Engineering Division, King Abdullah University of Science and Technology, Thuwal 23955-6900, Saudi Arabia*

Senfu Zhang − *Physical Science and Engineering Division, King Abdullah University of Science and Technology, Thuwal 23955-6900, Saudi Arabia; Key Laboratory for Magnetism and Magnetic Materials of Ministry of Education, Lanzhou University, Lanzhou 730000, P. R. China*

Shuai Yuan − *School of Mechanical and Electrical Engineering, Guilin University of Electronic Technology, Guilin 541004, P. R. China*

Minghui Qin − *Guangdong Provincial Key Laboratory of Optical Information Materials and Technology & Institute for Advanced Materials, South China Academy of Advanced Optoelectronics, South China Normal University, Guangzhou 510006, P. R. China*

Yongbing Xu − *School of Integrated Circuits, Guangdong University of Technology, Guangzhou 510006, China; School of Physics, Engineering and Technology, University of York, York YO10 5DD, U.K.*

Xingsen Gao − *Guangdong Provincial Key Laboratory of Optical Information Materials and Technology & Institute for Advanced Materials, South China Academy of Advanced Optoelectronics, South China Normal University, Guangzhou 510006, P. R. China;* orcid.org/0000-0002-2725-0785

Kai Liu − *Physics Department, Georgetown University, Washington, D.C. 20057, United States;* orcid.org/0000-0001-9413-6782

Zi Qiang Qiu − *Department of Physics, University of California at Berkeley, Berkeley, California 94720, United States;* orcid.org/0000-0003-0680-0714

Jun-Ming Liu − *Guangdong Provincial Key Laboratory of Optical Information Materials and Technology & Institute for Advanced Materials, South China Academy of Advanced Optoelectronics, South China Normal University, Guangzhou 510006, P. R. China; Laboratory of Solid State Microstructures and Innovation Center of Advanced Microstructures, Nanjing University, Nanjing 211102, P. R. China;* orcid.org/0000-0001-8988-8429

Complete contact information is available at: https://pubs.acs.org/10.1021/acsnano.3c09090

Author Contributions

C.L., J.W., and W.H. contributed equally to this work. C.L. and Z.H. conceived the idea and designed the experiments. Z.H., Y.P., and X.-X.Z. supervised the project. C.Z. performed the crystal growth. C.L. prepared the TEM samples and collected the atomic resolution HAADF-STEM images. C.L., W.H., and Z.H. performed the *in situ* LTEM experiments. S.Z., S.Y., J.W., and Z.H. conducted the micromagnetic simulations and the phase-field simulations. C.L., J.W., Z.H., and X.-X.Z. analyzed the data and wrote the manuscript with the help of C.Z., Y.X., M.Q., X.G., Y.P., Z.Q., K.L., and J.L. All authors contributed to the discussion of the results and improvement of the manuscript.

Notes

The authors declare no competing financial interest.

ACKNOWLEDGMENTS

This work was financially supported by the National Key Research and Development Program of China at grant No. 2020YFA0309300, King Abdullah University of Science and Technology (KAUST), Office of Sponsored Research (OSR) under Award Nos. ORA-CRG8-2019-4081 and ORA-CRG10-2021-4665, the National Natural Science Foundation of China (NSFC) at grant Nos. 12104197, 52271178, 52322108, 12304136, U22A20117, and 12241403, Guangdong Basic and Applied Basic Research Foundation at grant Nos. 2022A1515110863, 2023B1515020112, and 2023A1515010837. K.L. acknowledges support from the US National Science Foundation (DMR-2005108).

REFERENCES

(1) Fert, A.; Cros, V.; Sampaio, J. Skyrmions on the track. *Nat. Nanotechnol.* **2013**, *8* (3), 152−6.

(2) Nagaosa, N.; Tokura, Y. Topological properties and dynamics of magnetic skyrmions. *Nat. Nanotechnol.* **2013**, *8* (12), 899−911.

(3) Mühlbauer, S.; Binz, B.; Jonietz, F.; Pfleiderer, C.; Rosch, A.; Neubauer, A.; Georgii, R.; Böni, P. Skyrmion lattice in a chiral magnet. *Science* **2009**, *323* (5916), 915−919.

(4) Seki, S.; Yu, X. Z.; Ishiwata, S.; Tokura, Y. Observation of Skyrmions in a Multiferroic Material. *Science* **2012**, *336* (6078), 198−201.

(5) Yu, X. Z.; Kanazawa, N.; Onose, Y.; Kimoto, K.; Zhang, W. Z.; Ishiwata, S.; Matsui, Y.; Tokura, Y. Near room-temperature formation of a skyrmion crystal in thin-films of the helimagnet FeGe. *Nat. Mater.* **2011**, *10* (2), 106−9.

(6) Soumyanarayanan, A.; Raju, M.; Gonzalez Oyarce, A. L.; Tan, A. K. C.; Im, M. Y.; Petrovic, A. P.; Ho, P.; Khoo, K. H.; Tran, M.; Gan, C. K.; Ernult, F.; Panagopoulos, C. Tunable room-temperature magnetic skyrmions in Ir/Fe/Co/Pt multilayers. *Nat. Mater.* **2017**, *16* (9), 898−904.

(7) Jiang, W.; Chen, G.; Liu, K.; Zang, J.; te Velthuis, S. G. E.; Hoffmann, A. Skyrmions in magnetic multilayers. *Phys. Rep.* **2017**, *704*, 1−49.

(8) Hou, Z.; Ren, W.; Ding, B.; Xu, G.; Wang, Y.; Yang, B.; Zhang, Q.; Zhang, Y.; Liu, E.; Xu, F.; Wang, W.; Wu, G.; Zhang, X.; Shen, B.; Zhang, Z. Observation of Various and Spontaneous Magnetic Skyrmionic Bubbles at Room Temperature in a Frustrated Kagome Magnet with Uniaxial Magnetic Anisotropy. *Adv. Mater.* **2017**, *29* (29), No. 1701144.

(9) Yu, X.; Tokunaga, Y.; Taguchi, Y.; Tokura, Y. Variation of Topology in Magnetic Bubbles in a Colossal Magnetoresistive Manganite. *Adv. Mater.* **2017**, *29* (3), No. 1603958.

(10) Peng, L.; Zhang, Y.; Wang, W.; He, M.; Li, L.; Ding, B.; Li, J.; Sun, Y.; Zhang, X. G.; Cai, J.; Wang, S.; Wu, G.; Shen, B. Real-Space Observation of Nonvolatile Zero-Field Biskyrmion Lattice Generation in MnNiGa Magnet. *Nano Lett.* **2017**, *17* (11), 7075−7079.

(11) Yu, X.; Mostovoy, M.; Tokunaga, Y.; Zhang, W.; Kimoto, K.; Matsui, Y.; Kaneko, Y.; Nagaosa, N.; Tokura, Y. Magnetic stripes and skyrmions with helicity reversals. *Proc. Natl. Acad. Sci. U. S. A.* **2012**, *109* (23), 8856−8860.

(12) Jiang, W.; Zhang, X.; Yu, G.; Zhang, W.; Wang, X.; Jungfleisch, M. B.; Pearson, J. E.; Cheng, X.; Heinonen, O.; Wang, K. L.; et al. Direct observation of the skyrmion Hall effect. *Nat. Phys.* **2017**, *13* (2), 162−169.

(13) Zang, J.; Mostovoy, M.; Han, J. H.; Nagaosa, N. Dynamics of Skyrmion Crystals in Metallic Thin Films. *Phys. Rev. Lett.* **2011**, *107* (13), No. 136804.
(14) Raju, M.; Yagil, A.; Soumyanarayanan, A.; Tan, A. K. C.; Almoalem, A.; Ma, F.; Auslaender, O. M.; Panagopoulos, C. The evolution of skyrmions in Ir/Fe/Co/Pt multilayers and their topological Hall signature. *Nat. Commun.* **2019**, *10* (1), 696.
(15) Zhang, C.; Liu, C.; Zhang, J.; Yuan, Y.; Wen, Y.; Li, Y.; Zheng, D.; Zhang, Q.; Hou, Z.; Yin, G.; et al. Room Temperature Magnetic Skyrmions and Large Topological Hall Effect in Chromium Telluride Engineered by Self Intercalation. *Adv. Mater.* **2023**, *35* (1), No. 2205967.
(16) Kurumaji, T.; Nakajima, T.; Hirschberger, M.; Kikkawa, A.; Yamasaki, Y.; Sagayama, H.; Nakao, H.; Taguchi, Y.; Arima, T.-h.; Tokura, Y. Skyrmion lattice with a giant topological Hall effect in a frustrated triangular-lattice magnet. *Science* **2019**, *365* (6456), 914−918.
(17) Hou, Z.; Zhang, Q.; Zhang, X.; Xu, G.; Xia, J.; Ding, B.; Li, H.; Zhang, S.; Batra, N. M.; Costa, P.; Liu, E.; Wu, G.; Ezawa, M.; Liu, X.; Zhou, Y.; Zhang, X.; Wang, W. Current-Induced Helicity Reversal of a Single Skyrmionic Bubble Chain in a Nanostructured Frustrated Magnet. *Adv. Mater.* **2020**, *32* (1), No. e1904815.
(18) Wei, W.; Tang, J.; Wu, Y.; Wang, Y.; Jiang, J.; Li, J.; Soh, Y.; Xiong, Y.; Tian, M.; Du, H. Current-Controlled Topological Magnetic Transformations in a Nanostructured Kagome Magnet. *Adv. Mater.* **2021**, *33* (33), No. 2101610.
(19) Jonietz, F.; Mühlbauer, S.; Pfleiderer, C.; Neubauer, A.; Münzer, W.; Bauer, A.; Adams, T.; Georgii, R.; Böni, P.; Duine, R. A.; et al. Spin transfer torques in MnSi at ultralow current densities. *Science* **2010**, *330* (6011), 1648−1651.
(20) Lemesh, I.; Litzius, K.; Böttcher, M.; Bassirian, P.; Kerber, N.; Heinze, D.; Zázvorka, J.; Büttner, F.; Caretta, L.; Mann, M.; Weigand, M.; Finizio, S.; Raabe, J.; Im, M.-Y.; Stoll, H.; Schütz, G.; Dupé, B.; Kläui, M.; Beach, G. S. D. Current-Induced Skyrmion Generation through Morphological Thermal Transitions in Chiral Ferromagnetic Heterostructures. *Adv. Mater.* **2018**, *30* (49), No. 1805461.
(21) Jiang, W.; Upadhyaya, P.; Zhang, W.; Yu, G.; Jungfleisch, M. B.; Fradin, F. Y.; Pearson, J. E.; Tserkovnyak, Y.; Wang, K. L.; Heinonen, O.; et al. Blowing magnetic skyrmion bubbles. *Science* **2015**, *349* (6245), 283−286.
(22) Yu, X. Z.; Morikawa, D.; Nakajima, K.; Shibata, K.; Kanazawa, N.; Arima, T.; Nagaosa, N.; Tokura, Y. Motion tracking of 80-nm-size skyrmions upon directional current injections. *Science Advances* **2020**, *6* (25), No. eaaz9744.
(23) Yu, X. Z.; Kanazawa, N.; Zhang, W. Z.; Nagai, T.; Hara, T.; Kimoto, K.; Matsui, Y.; Onose, Y.; Tokura, Y. Skyrmion flow near room temperature in an ultralow current density. *Nat. Commun.* **2012**, *3*, 988.
(24) Iwasaki, J.; Mochizuki, M.; Nagaosa, N. Current-induced skyrmion dynamics in constricted geometries. *Nat. Nanotechnol.* **2013**, *8* (10), 742.
(25) Zhao, X.; Wang, S.; Wang, C.; Che, R. Thermal effects on current-related skyrmion formation in a nanobelt. *Appl. Phys. Lett.* **2018**, *112* (21), 212403.
(26) Schott, M.; Bernand-Mantel, A.; Ranno, L.; Pizzini, S.; Vogel, J.; Béa, H.; Baraduc, C.; Auffret, S.; Gaudin, G.; Givord, D. The Skyrmion Switch: Turning Magnetic Skyrmion Bubbles on and off with an Electric Field. *Nano Lett.* **2017**, *17* (5), 3006−3012.
(27) Bhattacharya, D.; Razavi, S. A.; Wu, H.; Dai, B.; Wang, K. L.; Atulasimha, J. Creation and annihilation of non-volatile fixed magnetic skyrmions using voltage control of magnetic anisotropy. *Nature Electronics* **2020**, *3* (9), 539−545.
(28) Hsu, P.-J.; Kubetzka, A.; Finco, A.; Romming, N.; von Bergmann, K.; Wiesendanger, R. Electric-field-driven switching of individual magnetic skyrmions. *Nat. Nanotechnol.* **2017**, *12* (2), 123−126.
(29) Dai, B.; Wu, D.; Razavi, S. A.; Xu, S.; He, H.; Shu, Q.; Jackson, M.; Mahfouzi, F.; Huang, H.; Pan, Q.; Cheng, Y.; Qu, T.; Wang, T.; Tai, L.; Wong, K.; Kioussis, N.; Wang, K. L. Electric field manipulation of spin chirality and skyrmion dynamic. *Science Advances* **2023**, *9* (7), No. eade6836.
(30) Berruto, G.; Madan, I.; Murooka, Y.; Vanacore, G. M.; Pomarico, E.; Rajeswari, J.; Lamb, R.; Huang, P.; Kruchkov, A. J.; Togawa, Y.; LaGrange, T.; McGrouther, D.; Rønnow, H. M.; Carbone, F. Laser-Induced Skyrmion Writing and Erasing in an Ultrafast Cryo-Lorentz Transmission Electron Microscope. *Phys. Rev. Lett.* **2018**, *120* (11), No. 117201.
(31) Psaroudaki, C.; Loss, D. Skyrmions Driven by Intrinsic Magnons. *Phys. Rev. Lett.* **2018**, *120* (23), No. 237203.
(32) Wang, Z.; Guo, M.; Zhou, H.-A.; Zhao, L.; Xu, T.; Tomasello, R.; Bai, H.; Dong, Y.; Je, S.-G.; Chao, W.; Han, H.-S.; Lee, S.; Lee, K.-S.; Yao, Y.; Han, W.; Song, C.; Wu, H.; Carpentieri, M.; Finocchio, G.; Im, M.-Y.; Lin, S.-Z.; Jiang, W. Thermal generation, manipulation and thermoelectric detection of skyrmions. *Nature Electronics* **2020**, *3* (11), 672−679.
(33) Chen, G.; Ophus, C.; Quintana, A.; Kwon, H.; Won, C.; Ding, H.; Wu, Y.; Schmid, A. K.; Liu, K. Reversible writing/deleting of magnetic skyrmions through hydrogen adsorption/desorption. *Nat. Commun.* **2022**, *13* (1), 1350.
(34) Chen, G.; Mascaraque, A.; Jia, H.; Zimmermann, B.; Robertson, M.; Conte, R. L.; Hoffmann, M.; González Barrio, M. A.; Ding, H.; Wiesendanger, R.; Michel, E. G.; Blügel, S.; Schmid, A. K.; Liu, K. Large Dzyaloshinskii-Moriya interaction induced by chemisorbed oxygen on a ferromagnet surface. *Science Advances* **2020**, *6* (33), No. eaba4924.
(35) Shibata, K.; Iwasaki, J.; Kanazawa, N.; Aizawa, S.; Tanigaki, T.; Shirai, M.; Nakajima, T.; Kubota, M.; Kawasaki, M.; Park, H. S.; Shindo, D.; Nagaosa, N.; Tokura, Y. Large anisotropic deformation of skyrmions in strained crystal. *Nat. Nanotechnol.* **2015**, *10* (7), 589−92.
(36) Wang, Y.; Wang, L.; Xia, J.; Lai, Z.; Tian, G.; Zhang, X.; Hou, Z.; Gao, X.; Mi, W.; Feng, C.; Zeng, M.; Zhou, G.; Yu, G.; Wu, G.; Zhou, Y.; Wang, W.; Zhang, X.-x.; Liu, J. Electric-field-driven non-volatile multi-state switching of individual skyrmions in a multiferroic heterostructure. *Nat. Commun.* **2020**, *11* (1), 3577.
(37) Wang, J.; Shi, Y.; Kamlah, M. Uniaxial strain modulation of the skyrmion phase transition in ferromagnetic thin films. *Phys. Rev. B* **2018**, *97* (2), No. 024429.
(38) Wang, J.; Zhang, J. A real-space phase field model for the domain evolution of ferromagnetic materials. *International Journal of Solids and Structures* **2013**, *50* (22), 3597−3609.
(39) Hu, J.-M.; Yang, T.; Chen, L.-Q. Strain-mediated voltage-controlled switching of magnetic skyrmions in nanostructures. *npj Computational Materials* **2018**, *4* (1), 62.
(40) Chacon, A.; Bauer, A.; Adams, T.; Rucker, F.; Brandl, G.; Georgii, R.; Garst, M.; Pfleiderer, C. Uniaxial pressure dependence of magnetic order in MnSi. *Phys. Rev. Lett.* **2015**, *115* (26), No. 267202.
(41) Hu, Y.; Lan, X.; Wang, B. Nonlinear emergent elasticity and structural transitions of a skyrmion crystal under uniaxial distortion. *Phys. Rev. B* **2019**, *99* (21), No. 214412.
(42) Sukhanov, A. S.; Vir, P.; Heinemann, A.; Nikitin, S. E.; Kriegner, D.; Borrmann, H.; Shekhar, C.; Felser, C.; Inosov, D. S. Giant enhancement of the skyrmion stability in a chemically strained helimagnet. *Phys. Rev. B* **2019**, *100* (18), No. 180403.
(43) Feng, C.; Meng, F.; Wang, Y.; Jiang, J.; Mehmood, N.; Cao, Y.; Lv, X.; Yang, F.; Wang, L.; Zhao, Y.; Xie, S.; Hou, Z.; Mi, W.; Peng, Y.; Wang, K.; Gao, X.; Yu, G.; Liu, J. Field-Free Manipulation of Skyrmion Creation and Annihilation by Tunable Strain Engineering. *Adv. Funct. Mater.* **2021**, *31* (14), No. 2008715.
(44) Nii, Y.; Nakajima, T.; Kikkawa, A.; Yamasaki, Y.; Ohishi, K.; Suzuki, J.; Taguchi, Y.; Arima, T.; Tokura, Y.; Iwasa, Y. Uniaxial stress control of skyrmion phase. *Nat. Commun.* **2015**, *6*, 8539.
(45) Shi, Y.; Wang, J. Stabilizing skyrmions by non-uniform strain in ferromagnetic thin films without a magnetic field. *Phys. Rev. B* **2018**, *97* (22), 224428.
(46) Seki, S.; Okamura, Y.; Shibata, K.; Takagi, R.; Khanh, N. D.; Kagawa, F.; Arima, T.; Tokura, Y. Stabilization of magnetic skyrmions by uniaxial tensile strain. *Phys. Rev. B* **2017**, *96* (22), No. 220404.
(47) Wang, J. Mechanical Control of Magnetic Order: From Phase Transition to Skyrmions. *Annu. Rev. Mater. Res.* **2019**, *49* (1), 361−388.

https://doi.org/10.1021/acsnano.3c09090
ACS Nano 2024, 18, 761−769

(48) Hu, J.-M.; Yang, T.; Chen, L.-Q. Stability and dynamics of skyrmions in ultrathin magnetic nanodisks under strain. *Acta Mater.* **2020**, *183*, 145−154.
(49) Cheng, Y.; Dong, G.; Li, Y.; Yang, G.; Zhang, B.; Guan, M.; Zhou, Z.; Liu, M. Strain Modulation of Perpendicular Magnetic Anisotropy in Wrinkle-Patterned (Co/Pt)5/BaTiO3Magnetoelectric Heterostructures. *ACS Nano* **2022**, *16* (7), 11291−11299.
(50) Kong, D.; Kovács, A.; Charilaou, M.; Zheng, F.; Wang, L.; Han, X.; Dunin-Borkowski, R. E. Direct observation of tensile-strain-induced nanoscale magnetic hardening. *Nat. Commun.* **2023**, *14* (1), 3963.
(51) Tomasello, R.; Komineas, S.; Siracusano, G.; Carpentieri, M.; Finocchio, G. Chiral skyrmions in an anisotropy gradient. *Phys. Rev. B* **2018**, *98* (2), No. 024421.
(52) Gorshkov, I. O.; Gorev, R. V.; Sapozhnikov, M. V.; Udalov, O. G. DMI-Gradient-Driven Skyrmion Motion. *ACS Applied Electronic Materials* **2022**, *4* (7), 3205−3211.
(53) Xing, X.; Zhou, Y. Skyrmion motion and partitioning of domain wall velocity driven by repulsive interactions. *Communications Physics* **2022**, *5* (1), 241.
(54) Vansteenkiste, A.; Leliaert, J.; Dvornik, M.; Helsen, M.; Garcia-Sanchez, F.; Van Waeyenberge, B. The design and verification of MuMax3. *AIP Advances* **2014**, *4* (10), No. 107133.

https://doi.org/10.1021/acsnano.3c09090
ACS Nano 2024, 18, 761−769